NANO LETTERS
Cite This: Nano Lett. 2019, 19, 3221−3228
Letter
pubs.acs.org/NanoLett

Length-Dependent Evolution of Type II Heterojunctions in Bottom-Up-Synthesized Graphene Nanoribbons

Daniel J. Rizzo,[†,#] Meng Wu,[†,#] Hsin-Zon Tsai,[†,⊥] Tomas Marangoni,[‡] Rebecca A. Durr,[‡] Arash A. Omrani,[†] Franklin Liou,[†] Christopher Bronner,[†] Trinity Joshi,[†] Giang D. Nguyen,[†] Griffin F. Rodgers,[†] Won-Woo Choi,[†] Jakob H. Jørgensen,[†] Felix R. Fischer,*[,†,‡,§,∥] Steven G. Louie,*[,†,§] and Michael F. Crommie*[,†,§,∥]

[†]Department of Physics and [‡]Department of Chemistry, University of California, Berkeley, California 94720, United States
[§]Materials Sciences Division, Lawrence Berkeley National Laboratory, Berkeley, California 94720, United States
[∥]Kavli Energy NanoSciences Institute, University of California Berkeley, Berkeley, California 94720, United States

Supporting Information

ABSTRACT: The ability to tune the band-edge energies of bottom-up graphene nanoribbons (GNRs) via edge dopants creates new opportunities for designing tailor-made GNR heterojunctions and related nanoscale electronic devices. Here we report the local electronic characterization of type II GNR heterojunctions composed of two different nitrogen edge-doping configurations (carbazole and phenanthridine) that separately exhibit electron-donating and electron-withdrawing behavior. Atomically resolved structural characterization of phenanthridine/carbazole GNR heterojunctions was performed using bond-resolved scanning tunneling microscopy and noncontact atomic force microscopy. Scanning tunneling spectroscopy and first-principles calculations reveal that carbazole and phenanthridine dopant configurations induce opposite upward and downward orbital energy shifts owing to their different electron affinities. The magnitude of the energy offsets observed in carbazole/phenanthridine heterojunctions is dependent on the length of the GNR segments comprising each heterojunction with longer segments leading to larger heterojunction energy offsets. Using a new on-site energy analysis based on Wannier functions, we find that the origin of this behavior is a charge transfer process that reshapes the electrostatic potential profile over a long distance within the GNR heterojunction.

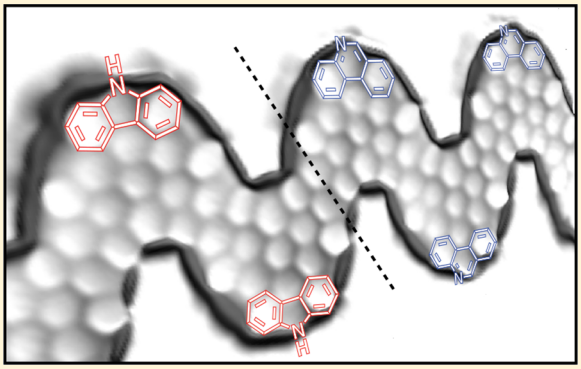

KEYWORDS: *Graphene nanoribbons (GNRs), molecular electronics, scanning tunneling microscopy (STM), scanning tunneling spectroscopy (STS), density functional theory (DFT), charge transfer, heterojunction, bottom-up*

Graphene nanoribbons (GNRs) are one-dimensional (1D) strips of graphene whose electronic structure can be precisely tuned through modification of GNR width,[1−6] edge structure,[1,7−9] topological states,[10,11] and dopant density and position.[12−18] Edge dopants have been shown to lead to energy downshifts in the band alignment of different GNRs, allowing fabrication of bottom-up heterojunctions (HJs) between doped and undoped GNR segments.[18,19] HJ systems explored to date have mostly consisted of random GNR segment lengths fused at a HJ interface[19,20] and there has been no systematic study of the dependence of HJ band offsets on constituent GNR segment lengths. Such HJ band offsets are expected to be influenced by charge transfer, dopant electron affinity, ribbon edge symmetry, and the competition between electronic kinetic and potential energy (i.e., quantum confinement along the GNR segment length). GNR HJs differ from conventional macroscopic semiconductor junctions (e.g., p−n junctions) in that the two sides of a GNR HJ cannot be treated as separate semi-infinite reservoirs with isolated electronic structure joined only through a well-defined depletion region where dopant-induced charge transfer occurs. The delocalized nature of π-orbitals along the GNR backbone and the microscopically confined nature of each GNR segment suggests that the concept of HJs in 1D GNR systems requires closer scrutiny.

In order to explore length-dependent behavior in GNR HJs, we have characterized the local electronic properties of bottom-up fabricated GNR HJs that incorporate both electron-withdrawing impurities (which lead to band edge downshifts) and electron-donating impurities (which lead to band edge upshifts). GNR HJs having different segment lengths were grown from a single methyl-carbazole edge-

Received: February 20, 2019
Revised: April 3, 2019
Published: April 19, 2019

DOI: 10.1021/acs.nanolett.9b00758
Nano Lett. 2019, 19, 3221−3228

functionalized precursor that spontaneously forms either electron-withdrawing phenanthridine moieties or electron-donating carbazole moieties during on-surface synthesis,[21] resulting in different HJ segment lengths. Noncontact atomic force microscopy (nc-AFM) and bond-resolved scanning tunneling microscopy (BRSTM) were used to identify local dopant configurations in conjunction with scanning tunneling spectroscopy (STS) to characterize local GNR HJ electronic structure. We observe that the HJ energy offset (i.e., the difference in band edge energy across a GNR HJ interface for either the conduction or valence band) depends strongly on the local dopant sequence. Band edge energies shift progressively upward for longer electron-donating HJ segments and progressively downward for longer electron-withdrawing segments, leading to energy offsets that increase with HJ segment length.

By using a novel Wannier-function-based approach to characterize the site-dependent energy profile, we find that this energy offset evolution originates from charge transfer across HJ interfaces that becomes progressively more dominant as HJ segment lengths decrease. Contrary to the role of charge transfer in typical three-dimensional macroscopic p−n junctions, molecular-scale charge transfer in type II GNR HJs reduces the intrinsic energy offset between short GNR segments with different electron affinities. Reduction of the energy offset in 1D HJs with very long segments is not significant due to the decay of the interfacial dipole potential, but when the segment size is comparable to the interfacial region then band alignment becomes size-dependent and the interfacial charge transfer reshapes the band edge energies of the whole system.

Results and Discussion. Nitrogen-doped chevron-type GNR heterojunctions were synthesized under ultrahigh vacuum (UHV) conditions from molecular precursors (Figure 1a) following standard sequential radical step-growth polymerization/cyclodehydrogenation protocols on Au(111).[22] In addition to the usual polymerization/cyclodehydrogenation processes, this synthesis also results in a spontaneous edge reconstruction of the methyl-carbazole moiety that can yield formation of either carbazole or phenanthridine in the fully formed GNR (Figure 1a).[21] Resulting GNRs thus exhibit nitrogen edge-impurities bound in either five-membered rings resembling carbazole (an electron-donating moiety[23]) or six-membered rings resembling phenanthridine (an electron-withdrawing moiety[23]) in a 2:3 ratio, as seen in our bond-resolved STM (BRSTM) images (Figure 1b). These doped-GNR building blocks (each arising from the same molecular precursor) will henceforth be referred to as 5-blocks (i.e., monomer segments containing a single carbazole group) and 6-blocks (monomer segments containing a single phenanthridine group) due to the number of atoms in the central ring of the dopant group. We used BRSTM[18] to distinguish 5-blocks from 6-blocks in GNR heterostructures because it allows both rapid structural screening and STM spectroscopic characterization without having to switch to noncontact AFM (nc-AFM) mode (we confirmed that BRSTM-based structural assignment of 5-membered and 6-membered rings are consistent with nc-AFM structural assignments (SI, Figure S1)).

Carbazole- and phenanthridine-functionalized GNR segments showed electronic structure differences that depend strongly on the local sequences of 5-blocks and 6-blocks. Using the convention of identifying the LDOS peaks bracketing E_F as

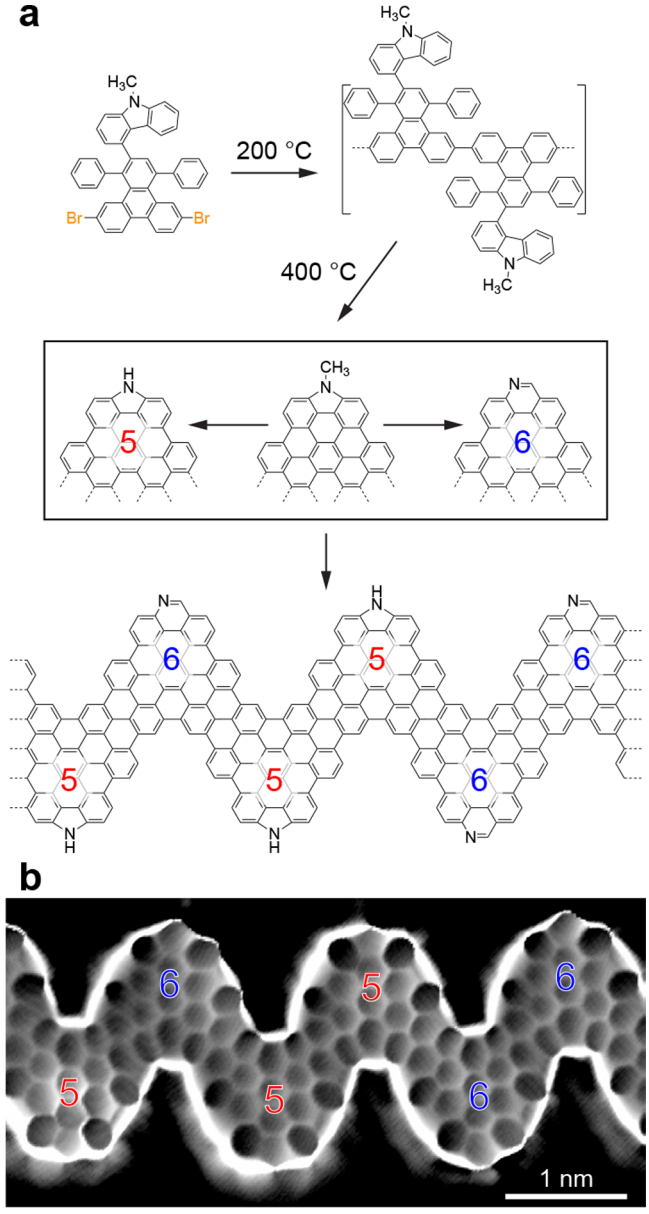

Figure 1. Bottom-up fabrication of carbazole (5)/phenanthridine (6) edge-functionalized GNR heterostructures. (a) Schematic representation of two-step bottom-up synthesis of GNR heterostructures on Au(111) via radical step-growth polymerization followed by cyclodehydrogenation/edge reconstruction. (b) BRSTM image of typical GNR heterostructure showing sequences of carbazole (5) and phenanthridine (6) edge functionalization (V_s = +20 mV, I_t = 40 pA, f = 401 Hz, V_{ac} = 20 mV, T = 4.5 K).

the valence band edge (VBE) and conduction band edge (CBE),[2,3,18] we observe that the shortest GNR HJ segments (i.e., alternating 5- and 6-blocks) show no HJ energy offset whereas longer GNR HJ segments exhibit significant HJ energy offsets that result in staggered type II HJs. The two main factors determining the local electronic behavior of a given 5- or 6-block within a 5/6 GNR HJ segment are (i) whether it is a 5- or 6-block and (ii) the number of like nearest neighbors that it has. The size of the band edge energy shift (which is positive for 5-blocks and negative for 6-blocks) increases as the number of like nearest neighbors for a block in a HJ segment increases from zero (i.e., N = 0 blocks in HJ segments one block long) to two (i.e., N = 2 blocks in HJ segments three blocks long).

DOI: 10.1021/acs.nanolett.9b00758
Nano Lett. 2019, 19, 3221−3228

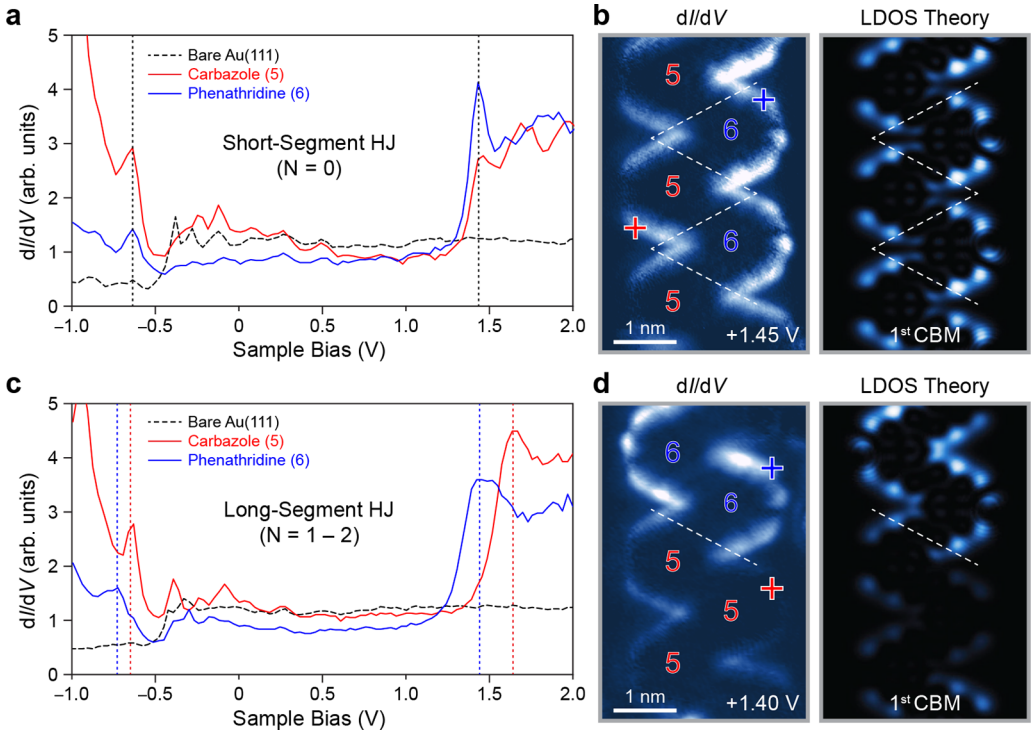

Figure 2. Scanning-tunneling spectroscopy of carbazole (5)/phenanthridine (6) edge-functionalized GNR heterojunctions (HJs). (a) dI/dV point spectra obtained on 5-block segment (red curve) and 6-block segment (blue curve) across HJ interface (white dashed line in (b)) for short-segment (N = 0) 5/6 GNR HJ (spectroscopy locations marked in (b)). Spectroscopy set point: V_s = 1.50 V, I_t = 25 pA. (b) Left: constant current dI/dV map at conduction band edge (CBE) for short segment 5/6 GNR HJ (5-blocks and 6-blocks are identified) (V_s = 1.45 V, I_t = 25 pA). Right: theoretical CBE LDOS map 4 Å above GNR plane for GNR having same 5/6 block sequence as shown on left. (c) Same as (a) but for a long-segment (N = 1−2) 5/6 GNR HJ (spectroscopy locations marked in (d)). (d) Same as (b) but for a long-segment (N = 1−2) 5/6 GNR HJ (V_s = 1.40 V, I_t = 15 pA). All dI/dV measurements collected with V_{AC} = 10 mV, f = 401 Hz, T = 4.5 K.

This behavior can be seen in Figure 2 which compares the spectroscopic energy offsets of GNR HJs having different segment lengths. Figure 2a shows STM dI/dV spectra measured on either side of a GNR HJ having the shortest possible segment length: just a single molecular block (i.e., an alternating superlattice of 5-blocks and 6-blocks (Figure 2b)). Spectra obtained on either side of the N = 0 HJ divide (marked by dashed white lines in Figure 2b) show nearly identical electronic structure both for 5-blocks and 6-blocks. VBE and CBE peaks line up almost exactly in this case, leading to a vanishing HJ energy offset. The situation is very different for HJs with longer GNR segments as seen in Figure 2c, which shows dI/dV spectra acquired across an N = 1−2 HJ interface bracketed by segments containing two 6-blocks and three 5-blocks (Figure 2d). A substantial energy shift is now observed for the spectrum recorded in the N = 2 5-block region (red curve) relative to that taken in the N = 1 6-block region (blue curve). The HJ energy offset is measured to be 0.07 eV for the VBE and 0.21 eV for the CBE. (Average spectroscopic energy shifts for different sequences are shown in the SI, Figure S2.)

The spatial distribution of HJ electronic wave functions can be seen in segment-length dependent dI/dV maps of 5/6 HJs. Figure 2b shows a dI/dV map taken at the CBE (1.45 V) of the short-segment (N = 0) 5/6 HJ system. A general hallmark of HJs having nonzero energy offsets is spatial localization of band edge states to just one side of the HJ interface.[18,24] The absence of such localization in the N = 0 HJ reflects a suppressed energy offset between 5- and 6-blocks in short-segment HJs (differences in edge nodal structure can be seen between the 5- and 6-blocks, but there is no significant difference in wave function magnitude across the HJ interface). The situation is quite different for HJs made from longer GNR segments, as seen in the dI/dV map of Figure 2d obtained at the CBE of the N = 1−2 HJ (1.40 V). Here the 6-block segment (which is two blocks long) is markedly brighter than the 5-block segment (which is three blocks long). This shows the spatial localization of the CBE state to one side of this type II HJ and reflects the nonzero energy offset observed for 5/6 HJs with longer GNR segments. Similar results are obtained for occupied states (Figure S3) and other 5/6 HJs (Figure S4).

The central question that arises from these observations is why do short HJ segments result in no HJ energy offset (Figure 2a,b) whereas longer segments result in an increased energy offset (Figure 2c,d)? From previous work we know that 1D and 2D HJs are very different from their 3D counterparts since the field lines of interfacial dipoles in 1D and 2D are not confined to the narrow interface region as in the 3D case but rather leak into the vacuum region.[25−27] For sufficiently long 1D HJ segments, frontier molecular orbital theory suggests that a significant 5/6 HJ offset should exist since phenanthridine has a much higher electron affinity than carbazole (by ∼0.7 eV (see Table S1)), implying that 6-block electronic states should lie lower in energy than 5-block states. Such intuition bears out when DFT is used to calculate the electronic structure of "all carbazole" GNRs (i.e., having carbazole functionalization on every edge) compared to "all phenanthridine" GNRs (which have phenanthridine at every edge). As shown in Figures S5 and S6, the electronic structure of all-phenanthridine GNRs is shifted down in energy by 0.4 eV compared to all-carbazole

DOI: 10.1021/acs.nanolett.9b00758
Nano Lett. 2019, 19, 3221−3228

GNRs, suggesting that 5/6 HJs should have an energy offset of this order.

A very different theoretical result, however, is obtained for DFT simulations of short-segment 5/6 HJs, as shown in Figures S2 and S7. Here the LDOS can be seen for 5-block and 6-block regions in periodic HJs having segment lengths of one block, two blocks, and three blocks. For periodic GNRs where the segment length is only one block (the $N = 0$ case), the energy offset between adjacent 5- and 6-blocks collapses nearly to zero. As the segment length increases the HJ energy offset between 5-block and 6-block regions grows, in agreement with our experimental observations (Figures 2, S2). These simulations confirm that the electronic structure of 5/6 HJs depends on segment-length, but they do not uncover the physical mechanism by which this occurs because LDOS distributions cannot directly show how charge transfers across HJ interfaces.

To understand the role played by charge transfer in determining the behavior of 5/6 GNR HJs, we calculated the Hirshfeld-I local charge transfer for HJs having different segment lengths (Figure 3). This technique yields the difference in charge around each atom in a GNR compared to that same atom if it were isolated (see SI, Figure S8 for further details). The main result of this analysis is that the magnitude of charge transfer to a 5- or 6-block in a GNR depends on how many like nearest neighbors it has. For example, blocks with no like nearest neighbors ($N = 0$ blocks) experience the most net charge transfer per block. Blocks with a single like nearest neighbor ($N = 1$ blocks) experience less net charge transfer per block, and blocks with two like nearest neighbors ($N = 2$ blocks) experience the least overall charge transfer per block. This is not at first obvious from the Hirshfeld-I charge transfer plots in Figure 3 which show very strong local charge transfer at the nearly ionic C—H and C—N bonds near the GNR edge and weak charge transfer at covalent C—C bonds in the GNR interior. To understand the charge transfer between blocks we must add all of the charge differences within a boundary surrounding each block and compare the net total for each block. This procedure reveals that a net charge of −0.04|e| flows out of each 5-block and into each 6-block for short-segment $N = 0$ 5/6 HJs (Figure 3a). However, the charge transfer out of each block reduces to −0.03|e| for $N = 1$ 5-blocks in longer HJ segments (Figure 3b). This result is intuitive since an $N = 1$ block has one like nearest neighbor which reduces the overall difference in electron affinity that such a block experiences with adjacent groups compared to the $N = 0$ case (thus reducing the main driving force for charge transfer). Similarly, $N = 2$ blocks at the center of even longer HJ segments experience a more uniform electron affinity environment and therefore exhibit even less charge transfer (±0.01|e|, Figure 3c).

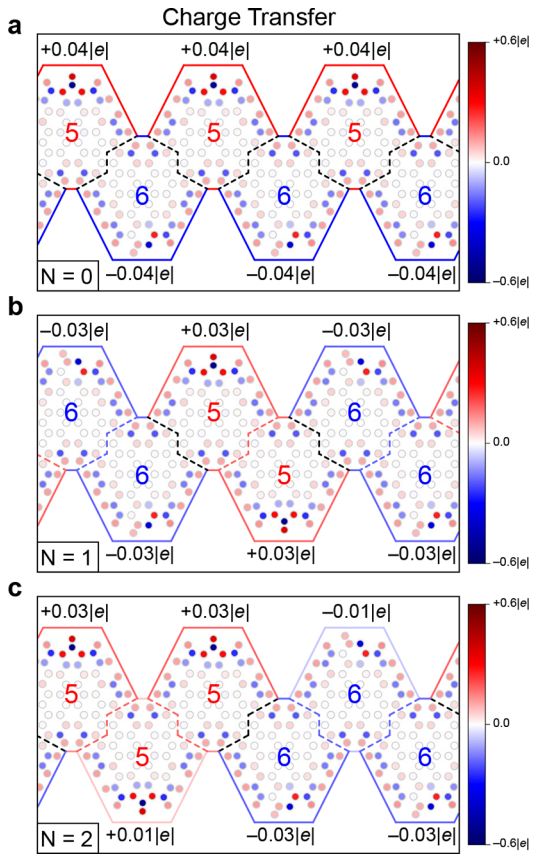

Figure 3. Hirshfeld-I charge analysis of (a) short-segment (blocks have no like neighbors, $N = 0$), (b) medium-segment (blocks have one like neighbor, $N = 1$), and (c) long-segment (blocks have two like neighbors, $N = 2$) carbazole (5)/phenanthridine (6) GNR heterojunctions showing charge transfer between 5-blocks and 6-blocks. The net charges are summed over each 5- and 6-block within the heptagon-like boundaries. The 5-blocks exhibit overall positive charge accumulation while 6-blocks exhibit overall negative charge accumulation. Black dashed lines identify HJ interfaces. Dashed lines delimit each block.

Charge transfer by itself, however, does not directly explain the results of our STM spectroscopy since we must still understand how this affects the GNR LDOS, which is what we are actually measuring. Untangling how different factors (such as electrostatics, kinetic energy, and exchange correlation) impact LDOS behavior in a large heterogeneous system such as a GNR HJ is nontrivial and typically depends on many model-dependent assumptions. To avoid such ambiguities, we here introduce a first-principles method which allows local characterization of GNR HJ energetics by mapping k-space band energies onto real-space on-site energies. This technique is based on the following identity involving Wannier functions (see SI, Figure S9 for derivation)

$$\sum_{n=1}^{N} E_{n\Gamma} = \sum_{m=1}^{N} \left\langle W_m | \hat{H} | W_m \right\rangle \tag{1}$$

Here N is the number of carbon/nitrogen atoms in a GNR unit cell (as well as the total number of π-bands), and the left side of eq 1 sums band energies at the Γ point. $\hat{H}$ is the Hamiltonian of the system and the right side sums on-site energies for Wannier functions located at every carbon/nitrogen site within the GNR unit cell. This identity establishes a relation between offsets in electronic energy levels and local variations in the Wannier on-site energy term. Given the physically reasonable assumption that the band edge states shift in energy together with all the relevant π-states, we can then utilize eq 1 to access local band bending phenomena. This allows Wannier functions, which possess the symmetry of atomic orbitals, to serve as a local probe (having atomic resolution) of the electronic structure. The strength of this technique is that local energy offsets can then be broken down (through $\hat{H}$) into their constituent components such as the Hartree plus ionic term, kinetic energy, and the exchange-

DOI: 10.1021/acs.nanolett.9b00758
Nano Lett. 2019, 19, 3221−3228

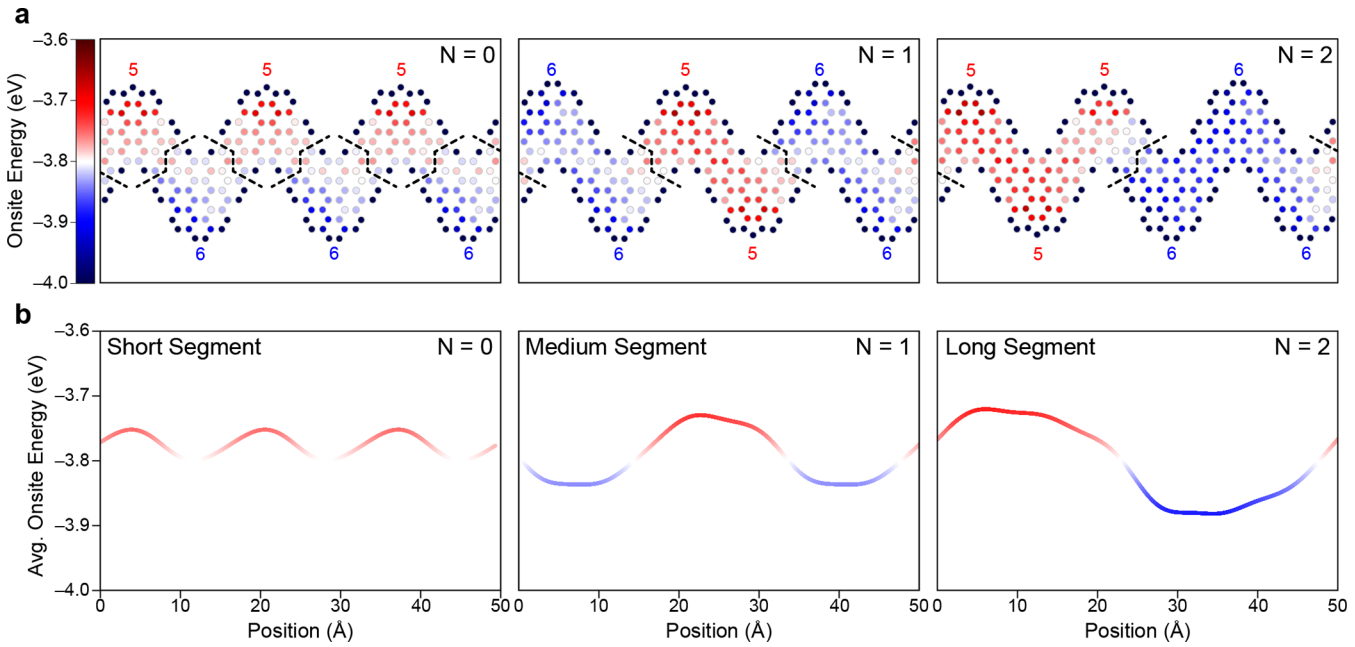

Figure 4. Wannier on-site energies for carbazole (5)/phenanthridine (6) edge-functionalized GNR heterojunctions (HJs). (a) Wannier on-site energies plotted for 5/6 GNR HJs having segment lengths of one (N = 0), two (N = 1), and three (N = 2). Black dashed lines identify HJ interfaces. (b) Spatially averaged on-site energies for interior carbon atoms (i.e., those not passivated by a hydrogen atom or bonded with a nitrogen atom) along the GNR backbone plotted as a function of distance. A spatial Gaussian broadening of 3 Å is applied. The HJ energy offset (peak-to-trough distance) increases with 5/6 HJ segment length.

correlation term in order to unravel the microscopic origins (such as charge transfer) of different LDOS features (see SI, Figure S10). This technique is an improvement over simply inspecting local mean-field potentials (e.g., V_{Hartree}, $V_{\text{xc.}}$) because the on-site energy does not fluctuate as strongly in space and encodes additional information about the electronic eigenstates.

To accomplish this analysis, we calculated the local on-site energies for the periodic N = 0, N = 1, and N = 2 HJ structures shown in Figure 3 using p_z-like Wannier functions. The resulting spatially resolved energy offsets are shown in Figure 4. The outermost edge carbon atoms exhibit near uniform low on-site energy, and nitrogen atom on-site energies are even lower due to their high electronegativity. Because the on-site energies of outer carbon and nitrogen atoms are dominated by nearly ionic C—H and C—N bonds, we focus on the interior carbon atoms where the bulk of the GNR band edge wave functions reside (Figure S11). The on-site energy map shows a spatial oscillation (Figure 4a) that has peaks in the 5-blocks and troughs in the 6-blocks (as expected from simple electron affinity considerations). This is most clearly seen in Figure 4b which shows a rolling average of the on-site energy for interior carbon atoms as a function of distance along the GNR backbone. The calculated HJ energy offset corresponds to the trough-to-peak energy difference in this curve as the HJ interface is crossed. This quantity increases as GNR HJ segments increase in length, consistent with our experimental data as shown in Figure 5. The small overestimation of the theoretical energy offsets compared to experiment is likely due to substrate-induced screening reducing the energy offsets of experimental 5/6 GNR HJs compared to simulated free-standing HJs.

The power of this new analysis comes from the fact that the physical origin of segment-length dependent 5/6 HJ energy offsets can now be revealed by decomposing the on-site energy

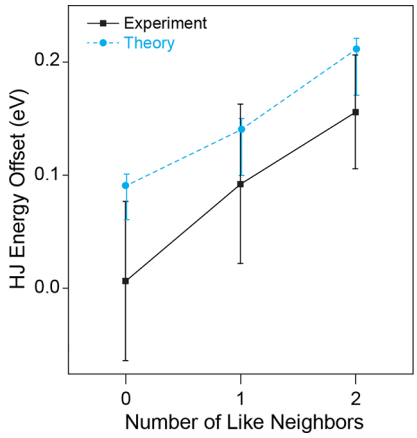

Figure 5. Comparison between experimental and theoretical heterojunction (HJ) energy offsets for carbazole (5)/phenanthridine (6) GNR HJs as a function of HJ segment length (indexed by number of like nearest neighbor blocks). The theoretical HJ energy offsets are the average difference between the peak and trough energies of the plots in Figure 4b while the experimental HJ energy offsets are the average energy shift of the VBE and CBE peaks measured in 5- and 6-blocks across 5/6 GNR HJ interfaces (SI, Figure S2). Uncertainties in the theory values arise from the range of energy offsets observed for different Gaussian averaging radii (1−5 Å) while uncertainties in the experimental values reflect the standard deviations of the respective experimental measurements.

(eq 1) into contributions from each component within a Kohn−Sham equation (i.e., kinetic energy, Hartree plus ionic potential, and exchange-correlation potential) through the following relations

$$\hat{H} = \sum_i \hat{H}_i = \hat{H}_{\text{K.E.}} + \hat{H}_{\text{Hartree+ion}} + \hat{H}_{\text{xc}} \quad (2)$$

DOI: 10.1021/acs.nanolett.9b00758
Nano Lett. 2019, 19, 3221−3228

$$\sum_{n=1}^{N} E_{n\Gamma} = \sum_{m=1}^{N} \sum_{i} \left\langle W_m | \hat{H}_i | W_m \right\rangle \quad (3)$$

A plot of the spatial dependence of each component in eqs 2 and 3 for 5/6 HJs of different segment length can be seen in Figure S10. Spatial variation in the electrostatic (Hartree+ion) term is seen to dominate the energy offset across HJ interfaces for all segment lengths with the spatial dependence of the kinetic energy and exchange-correlation terms being significantly smaller. This reveals that the segment-length dependent energy offsets observed in 5/6 GNR HJs can be attributed to electrostatic potential variations arising from charge transfer processes. Our observations are consistent with a physical regime for microscopic HJs where segment length is comparable to interfacial extent, and therefore band alignment across the HJ is sensitive to segment size as well as interfacial composition. In the extreme $N = 0$ case, the effect of charge transfer is seen to renormalize GNR HJ energy offsets so drastically that it almost completely offsets the intrinsic electron affinity differences of the constituents. This is quite different from 3D type II semiconductor p−n junction systems where interfacial charge transfer causes the HJ energy offset and interfacial band bending follows Anderson's rule.[27]

Conclusion. We have characterized the local electronic structure of GNR HJs that contain different nitrogen edge-dopant configurations exhibiting electron-donating and electron-withdrawing character. The difference in the electron affinities of these dopant groups leads to type II HJ behavior, and the magnitude of the HJ energy offset is observed to be proportional to HJ segment length. By analyzing intrablock charge transfer and local variations in on-site energies we have determined that GNR HJ band bending is not fixed for this class of 1D HJs and that charge transfer can completely offset intrinsic band alignment if HJ segment length is short enough. The new insights into nanoscale HJ electronic structure developed here should help facilitate the design and fabrication of future bottom-up GNR HJ devices and provide a general framework in which to characterize the electronic structure of heterogeneous nanoscale materials.

Methods. GNR heterostructures were grown on clean Au(111) thin films prepared using standard Ar^+ sputter/anneal cleaning cycles. GNR precursors (Figure 1a) were sublimed onto Au(111) held at 25 °C in ultrahigh vacuum from home-built Knudsen cell evaporators using a crucible temperature of 225 °C. After deposition, the surface temperature was ramped to 200 °C (≤2 K min^{-1}) and held for 30 min to induce radical-step growth polymerization, then ramped to 400 °C (≤2 K min^{-1}) and held for 30 min to induce cyclodehydrogenation. A characteristic overview of GNRs grown in this fashion is shown in Figure S12.

All STM experiments were performed using a commercial Omicron LT-STM/nc-AFM held at 4.5 K. A CO-functionalized W tip was used for all nc-AFM, BRSTM, and STS measurements. All experimental images were edited using WSxM software.[28] dI/dV measurements were recorded using a lock-in amplifier with modulation frequency of 401 Hz and modulation amplitude V_{rms} = 6−10 mV. dI/dV point spectra were recorded under open feedback loop conditions while dI/dV maps were collected under constant current conditions (constant height dI/dV maps yielded similar results after proper background subtraction (see SI, Figure S13)). BRSTM images were obtained by mapping the out-of-phase dI/dV signal collected during a low bias (10−20 mV) dI/dV map. Peak positions in point spectroscopy were determined by fitting Lorentzian distributions using Fityk[29] software. Each experimental data point presented in Figures 5 and S2d represents an average of at least 24 different spectra with at least 5 different tips. Before conducting STS experiments, all tips were repeatedly poked 1−2 nm into the clean Au(111) substrate until STS conducted on bare Au(111) yielded an otherwise featureless spectrum of the well-known Shockley surface state.[30]

First-principles calculations for carbazole and phenanthridine edge-functionalized GNR HJ's were performed using DFT at the LDA level implemented in the Quantum ESPRESSO package.[31] Norm-conserving pseudopotentials[32] were used with a planewave energy cutoff of 50 Ry. For the heterostructure calculations, we used free-standing periodic superlattices in which each unit cell was identical to the measured experimental heterojunction structure. All structures were fully relaxed until the force on each atom was smaller than 0.05 eV·$Å^{-1}$. All dangling σ-bonds were passivated with hydrogen atoms and LDOS calculations were performed at a height of 4 Å above the atomic plane. We simulated STS point spectra near the outer edges by taking a spatial 2D Gaussian weighting function with radius 2 Å and using it to sum energy-dependent LDOS near the edge (an energy broadening of 0.08 eV was employed in these calculations). On-site energies were calculated as the expectation values of the DFT Hamiltonian with respect to Wannier functions derived from carbon/nitrogen p_z orbitals and calculated from first-principles using the Wannier90 package.[33] Band structure calculated from a tight-binding model based on these Wannier functions was identical to that obtained from DFT calculations (Figure S9). Quasiparticle effects and substrate screening were included by performing G_0W_0 calculations[34] on chevron GNRs and utilizing an additional Thomas−Fermi screening term (see SI, Table S2).[6,35] GW calculations were performed using the BerkeleyGW code.[34,36] Our calculations show that the simulated 5/6 GNR HJ energy offsets are robust against many-body interactions and the presence of the gold substrate.

■ ASSOCIATED CONTENT

Supporting Information

The Supporting Information is available free of charge on the ACS Publications website at DOI: 10.1021/acs.nanolett.9b00758.

The SI contains a detailed summary of all theoretical calculations, including DFT, GW, Hirshfeld-I charge, and on-site energy analyses. Theoretical calculations of related GNR and molecular systems are also presented. Additional STM topography and dI/dV maps are presented in comparison to theory. A comparison of constant-height and constant-current dI/dV maps is presented, as well as a comparison between nc-AFM and BRSTM of GNR heterostructures (PDF)

■ AUTHOR INFORMATION

Corresponding Authors

*E-mail: (F.R.F) ffischer@berkeley.edu.
*E-mail: (S.G.L.) sglouie@berkeley.edu.
*E-mail: (M.F.C.) crommie@berkeley.edu.

ORCID

Christopher Bronner: 0000-0002-0083-5089

DOI: 10.1021/acs.nanolett.9b00758
Nano Lett. 2019, 19, 3221−3228

Trinity Joshi: 0000-0001-7566-3528
Felix R. Fischer: 0000-0003-4723-3111
Steven G. Louie: 0000-0003-0622-0170
Michael F. Crommie: 0000-0001-8246-3444

Present Address

[⊥]International Collaborative Laboratory of 2D Materials for Optoelectronic Science & Technology of Ministry of Education, Engineering Technology Research Center for 2D Material Information Function Devices and Systems of Guangdong Province, Shenzhen University, Shenzhen 518060, China.

Author Contributions

[#]D.J.R. and M.W. contributed equally to this work. D.J.R., H.-Z.T., A.A.O., F.L., C.B., T.J., G.D.N., G.F.R., W.-W.C., and J.H.J. performed STM and STS measurements. D.J.R. performed data analysis. M.W. performed theoretical calculations including DFT, GW, Hirshfeld-I charge, and on-site energy calculations to provide interpretation of STM data. T.M., R.A.D., and F.R.F. performed synthesis and structural characterization of GNR precursors and interpretation of STM data. M.F.C. supervised the experimental scanned probe measurements. S.G.L. supervised the calculations and theoretical analyses. M.F.C. and S.G.L. helped to interpret the results. All authors contributed to the scientific discussion and helped in writing the manuscript.

Notes

The authors declare no competing financial interest.

■ ACKNOWLEDGMENTS

Research supported by the U.S. Department of Energy (DOE), Office of Science, Basic Energy Sciences (BES), under the Nanomachine Program Award No. DE-AC02-05CH11231 (surface reaction characterization and DFT simulations), by the Office of Naval Research MURI award N00014-16-1-2921 (design of molecular building blocks, precursor synthesis, GNR bond-resolved imaging/spectroscopy), and by the National Science Foundation (NSF) under Grants DMR-1508412 (development of theory formalism) and DMR-1839098 (STM data analysis). Computational resources were provided by the DOE at Lawrence Berkeley National Laboratory's NERSC facility and the NSF through XSEDE resources at NICS. C.B. acknowledges support through the Fellowship Program of the German National Academy of Sciences Leopoldina under Grant LPDS 2014-09. A.A.O. acknowledges support from the Swiss National Science Foundation (SNSF) Postdoctoral Research Fellowship under Grant P2ELP2-151852. H.-Z.T. was financially supported by Shenzhen Peacock Plan (Grant No. 827-000113, KQJSCX20170727100802505, KQTD2016053112042971).

■ REFERENCES

(1) Son, Y.-W.; Cohen, M. L.; Louie, S. G. Energy Gaps in Graphene Nanoribbons. *Phys. Rev. Lett.* **2006**, *97*, 216803.
(2) Chen, Y.-C.; de Oteyza, D. G.; Pedramrazi, Z.; Chen, C.; Fischer, F. R.; Crommie, M. F. Tuning the Band Gap of Graphene Nanoribbons Synthesized from Molecular Precursors. *ACS Nano* **2013**, *7*, 6123−6128.
(3) Talirz, L.; Söde, H.; Dumslaff, T.; Wang, S.; Sanchez-Valencia, J. R.; Liu, J.; Shinde, P.; Pignedoli, C. A.; Liang, L.; Meunier, V.; Plumb, N. C.; Shi, M.; Feng, X.; Narita, A.; Müllen, K.; Fasel, R.; Ruffieux, P. On-Surface Synthesis and Characterization of 9-Atom Wide Armchair Graphene Nanoribbons. *ACS Nano* **2017**, *11*, 1380−1388.
(4) Kimouche, A.; Ervasti, M. M.; Drost, R.; Halonen, S.; Harju, A.; Joensuu, P. M.; Sainio, J.; Liljeroth, P. Ultra-narrow metallic armchair graphene nanoribbons. *Nat. Commun.* **2015**, *6*, 10177.
(5) Ruffieux, P.; Cai, J.; Plumb, N. C.; Patthey, L.; Prezzi, D.; Ferretti, A.; Molinari, E.; Feng, X.; Müllen, K.; Pignedoli, C. A.; Fasel, R. Electronic Structure of Atomically Precise Graphene Nanoribbons. *ACS Nano* **2012**, *6*, 6930−6935.
(6) Yang, L.; Park, C.-H.; Son, Y.-W.; Cohen, M. L.; Louie, S. G. Quasiparticle Energies and Band Gaps in Graphene Nanoribbons. *Phys. Rev. Lett.* **2007**, *99*, 186801.
(7) Ruffieux, P.; Wang, S.; Yang, B.; Sánchez-Sánchez, C.; Liu, J.; Dienel, T.; Talirz, L.; Shinde, P.; Pignedoli, C. A.; Passerone, D.; Dumslaff, T.; Feng, X.; Müllen, K.; Fasel, R. On-surface synthesis of graphene nanoribbons with zigzag edge topology. *Nature* **2016**, *531*, 489.
(8) Liu, J.; Li, B.-W.; Tan, Y.-Z.; Giannakopoulos, A.; Sanchez-Sanchez, C.; Beljonne, D.; Ruffieux, P.; Fasel, R.; Feng, X.; Müllen, K. Toward Cove-Edged Low Band Gap Graphene Nanoribbons. *J. Am. Chem. Soc.* **2015**, *137*, 6097−6103.
(9) Yazyev, O. V.; Capaz, R. B.; Louie, S. G. Theory of magnetic edge states in chiral graphene nanoribbons. *Phys. Rev. B: Condens. Matter Mater. Phys.* **2011**, *84*, 115406.
(10) Rizzo, D. J.; Veber, G.; Cao, T.; Bronner, C.; Chen, T.; Zhao, F.; Rodriguez, H.; Louie, S. G.; Crommie, M. F.; Fischer, F. R. Topological band engineering of graphene nanoribbons. *Nature* **2018**, *560*, 204−208.
(11) Gröning, O.; Wang, S.; Yao, X.; Pignedoli, C. A.; Borin Barin, G.; Daniels, C.; Cupo, A.; Meunier, V.; Feng, X.; Narita, A.; Müllen, K.; Ruffieux, P.; Fasel, R. Engineering of robust topological quantum phases in graphene nanoribbons. *Nature* **2018**, *560*, 209−213.
(12) Vo, T. H.; Perera, U. G. E.; Shekhirev, M.; Mehdi Pour, M.; Kunkel, D. A.; Lu, H.; Gruverman, A.; Sutter, E.; Cotlet, M.; Nykypanchuk, D.; Zahl, P.; Enders, A.; Sinitskii, A.; Sutter, P. Nitrogen-Doping Induced Self-Assembly of Graphene Nanoribbon-Based Two-Dimensional and Three-Dimensional Metamaterials. *Nano Lett.* **2015**, *15*, 5770−5777.
(13) Bronner, C.; Stremlau, S.; Gille, M.; Brauße, F.; Haase, A.; Hecht, S.; Tegeder, P. Aligning the Band Gap of Graphene Nanoribbons by Monomer Doping. *Angew. Chem.* **2013**, *125*, 4518−4521.
(14) Nguyen, G. D.; Toma, F. M.; Cao, T.; Pedramrazi, Z.; Chen, C.; Rizzo, D. J.; Joshi, T.; Bronner, C.; Chen, Y.-C.; Favaro, M.; Louie, S. G.; Fischer, F. R.; Crommie, M. F. Bottom-Up Synthesis of N = 13 Sulfur-Doped Graphene Nanoribbons. *J. Phys. Chem. C* **2016**, *120*, 2684−2687.
(15) Cloke, R. R.; Marangoni, T.; Nguyen, G. D.; Joshi, T.; Rizzo, D. J.; Bronner, C.; Cao, T.; Louie, S. G.; Crommie, M. F.; Fischer, F. R. Site-Specific Substitutional Boron Doping of Semiconducting Armchair Graphene Nanoribbons. *J. Am. Chem. Soc.* **2015**, *137*, 8872−8875.
(16) Kawai, S.; Saito, S.; Osumi, S.; Yamaguchi, S.; Foster, A. S.; Spijker, P.; Meyer, E. Atomically controlled substitutional boron-doping of graphene nanoribbons. *Nat. Commun.* **2015**, *6*, 8098.
(17) Carbonell-Sanromà, E.; Hieulle, J.; Vilas-Varela, M.; Brandimarte, P.; Iraola, M.; Barragán, A.; Li, J.; Abadia, M.; Corso, M.; Sánchez-Portal, D.; Peña, D.; Pascual, J. I. Doping of Graphene Nanoribbons via Functional Group Edge Modification. *ACS Nano* **2017**, *11*, 7355−7361.
(18) Nguyen, G. D.; Tsai, H.-Z.; Omrani, A. A.; Marangoni, T.; Wu, M.; Rizzo, D. J.; Rodgers, G. F.; Cloke, R. R.; Durr, R. A.; Sakai, Y.; Liou, F.; Aikawa, A. S.; Chelikowsky, J. R.; Louie, S. G.; Fischer, F. R.; Crommie, M. F. Atomically precise graphene nanoribbon heterojunctions from a single molecular precursor. *Nat. Nanotechnol.* **2017**, *12*, 1077.
(19) Cai, J.; Pignedoli, C. A.; Talirz, L.; Ruffieux, P.; Söde, H.; Liang, L.; Meunier, V.; Berger, R.; Li, R.; Feng, X.; Müllen, K.; Fasel, R. Graphene nanoribbon heterojunctions. *Nat. Nanotechnol.* **2014**, *9*, 896.

DOI: 10.1021/acs.nanolett.9b00758
Nano Lett. 2019, 19, 3221−3228

(20) Chen, Y.-C.; Cao, T.; Chen, C.; Pedramrazi, Z.; Haberer, D.; de Oteyza, D. G.; Fischer, F. R.; Louie, S. G.; Crommie, M. F. Molecular bandgap engineering of bottom-up synthesized graphene nanoribbon heterojunctions. *Nat. Nanotechnol.* **2015**, *10*, 156.
(21) Marangoni, T.; Haberer, D.; Rizzo, D. J.; Cloke, R. R.; Fischer, F. R. Heterostructures through Divergent Edge Reconstruction in Nitrogen-Doped Segmented Graphene Nanoribbons. *Chem. - Eur. J.* **2016**, *22*, 13037−13040.
(22) Cai, J.; Ruffieux, P.; Jaafar, R.; Bieri, M.; Braun, T.; Blankenburg, S.; Muoth, M.; Seitsonen, A. P.; Saleh, M.; Feng, X.; Müllen, K.; Fasel, R. Atomically precise bottom-up fabrication of graphene nanoribbons. *Nature* **2010**, *466*, 470.
(23) Naghavi, S. S.; Gruhn, T.; Alijani, V.; Fecher, G. H.; Felser, C.; Medjanik, K.; Kutnyakhov, D.; Nepijko, S. A.; Schönhense, G.; Rieger, R.; et al. Theoretical study of new acceptor and donor molecules based on polycyclic aromatic hydrocarbons. *J. Mol. Spectrosc.* **2011**, *265*, 95−101.
(24) Tersoff, J. Theory of semiconductor heterojunctions: The role of quantum dipoles. *Phys. Rev. B: Condens. Matter Mater. Phys.* **1984**, *30*, 4874−4877.
(25) Zhang, J.; Xie, W.; Zhao, J.; Zhang, S. Band alignment of two-dimensional lateral heterostructures. *2D Mater.* **2017**, *4*, 015038.
(26) Léonard, F.; Tersoff, J. Role of Fermi-Level Pinning in Nanotube Schottky Diodes. *Phys. Rev. Lett.* **2000**, *84*, 4693−4696.
(27) Anderson, R. L. Germanium-gallium arsenide heterojunctions. *IBM J. Res. Dev.* **1960**, *4*, 283−287.
(28) Horcas, I.; Fernández, R.; Gómez-Rodríguez, J. M.; Colchero, J.; Gómez-Herrero, J.; Baro, A. M. WSXM: A software for scanning probe microscopy and a tool for nanotechnology. *Rev. Sci. Instrum.* **2007**, *78*, 013705.
(29) Wojdyr, M. Fityk: A general-purpose peak fitting program. *J. Appl. Crystallogr.* **2010**, *43*, 1126−1128.
(30) Chen, W.; Madhavan, V.; Jamneala, T.; Crommie, M. F. Scanning Tunneling Microscopy Observation of an Electronic Superlattice at the Surface of Clean Gold. *Phys. Rev. Lett.* **1998**, *80*, 1469−1472.
(31) Giannozzi, P.; Baroni, S.; Bonini, N.; Calandra, M.; Car, R.; Cavazzoni, C.; Ceresoli, D.; Chiarotti, G. L.; Cococcioni, M.; Dabo, I. QUANTUM ESPRESSO: a modular and open-source software project for quantum simulations of materials. *J. Phys.: Condens. Matter* **2009**, *21*, 395502.
(32) Troullier, N.; Martins, J. L. Efficient pseudopotentials for plane-wave calculations. *Phys. Rev. B: Condens. Matter Mater. Phys.* **1991**, *43*, 1993−2006.
(33) Mostofi, A. A.; Yates, J. R.; Lee, Y.-S.; Souza, I.; Vanderbilt, D.; Marzari, N. wannier90: A tool for obtaining maximally-localised Wannier functions. *Comput. Phys. Commun.* **2008**, *178*, 685−699.
(34) Hybertsen, M. S.; Louie, S. G. Electron correlation in semiconductors and insulators: Band gaps and quasiparticle energies. *Phys. Rev. B: Condens. Matter Mater. Phys.* **1986**, *34*, 5390−5413.
(35) Neaton, J. B.; Hybertsen, M. S.; Louie, S. G. Renormalization of Molecular Electronic Levels at Metal-Molecule Interfaces. *Phys. Rev. Lett.* **2006**, *97*, 216405.
(36) Deslippe, J.; Samsonidze, G.; Strubbe, D. A.; Jain, M.; Cohen, M. L.; Louie, S. G. BerkeleyGW: A massively parallel computer package for the calculation of the quasiparticle and optical properties of materials and nanostructures. *Comput. Phys. Commun.* **2012**, *183*, 1269−1289.

DOI: 10.1021/acs.nanolett.9b00758
Nano Lett. 2019, 19, 3221−3228